Ambient fabrication of efficient triple cation perovskite-based near-infrared light-emitting diodes

Xiaohang Guo,[1] **Ivy M. Asuo,**[1,2] **Alain Pignolet,**[2] **Riad Nechache,**[2] **and Sylvain G. Cloutier**[1,*]

[1] *École de Technologie Supérieure (ÉTS), Department of Electrical Engineering, 1100 rue Notre-Dame Ouest, Montréal (QC) H3C 1K3, Canada*
[2] *INRS- Centre for Energy, Materials and Telecommunication, 1650 Boul. Lionel Boulet, Varennes (QC), J3X 1S2, Canada*
[*] *SylvainG.Cloutier@etsmtl.ca*

Abstract: In addition to their widespread use as an outstanding light-harvesting material, solution-based organometallic halide perovskites have also recently emerged as a promising material for light-emitting diode (LED) applications. However, their stability under an ambient environment remains a challenge. Triple cation perovskites offer an appealing solution as it reduces the sensitivity to the processing conditions and improves the purity of the perovskite films. This work describes a facile ambient-processed thiocyanate-doped triple-cation perovskite $Cs_x(MA_{0.17}FA_{0.83})Pb_{(100-x)}(I_{0.83}Br_{0.17})_3$ used for high-performance perovskite-based LEDs with peak emission at 750 nm. Using the perovskite film tailoring technique by mixing DMF (N,N-Dimethylmethanamide) with perovskite precursor, we are able to reduce the perovskite grain size and optimize the film thickness while preserving its crystalline structure. With optimized processing techniques, we achieve a ~90% improvement of the perovskite LEDs external quantum efficiency (EQE) from ~3.1% to ~5.9%. We believe this triple cation perovskite synthesis approach and film tailoring technique yields excellent device performances and constitutes a significant step towards low-cost and efficient LEDs.

1. Introduction

Recently, solution-based organo-inorganic halide perovskite materials with a general chemical formula of ABX_3 have undergone remarkable developments. This is largely due to their promising electrical and optical properties, including high charge-carrier mobility, long free-carrier diffusion length, tunable bandgap, and high quantum yield largely used for solar energy-harvesting applications [1–9]. After just over a decade [10], these solution-processed perovskite-based solar cells now exceed 25% in power conversion efficiencies [11], and constitute one of the most promising candidates for low-cost renewable energy generation for the near future. In addition to their successful use in solar cells, these materials can also exhibit great performances for other optoelectronic device applications including lasers [12,13], photodetectors [14–16] and light-emitting diodes (LEDs) [17–22]. Their narrow and tunable emission, low exciton binding energies and low-cost processing are especially appealing for new generations of LEDs [18,23–31]. Generally, perovskite-based LEDs are fabricated using an intrinsic light-emitting active layer sandwiched between an electron injection layer (EIL) and a hole injection layer (HIL) [32]. When applying a forward bias, carriers are injected into the active layer, where electrons and holes can bind and recombine radiatively [25,33]. In order to improve the performance of these LED devices, uniform densely-packed and pinhole-free films with small crystallites are required [24,31,34–37]. The densely-packed and pinhole-free perovskite could the current leakage [38]. The Small crystal grain size is able to prevent the excitons or charge carriers

from diffusing away by facilitating the spatial confinement of the excitons as well as reduce the diffusion length; therefore, it would reduce the dissociation of the excitons [39,40]. In 2018, a dramatic improvement in external quantum efficiency (EQE) to reach 1.2%, was first reported using a blend of perovskite and polyimide precursor dielectric (PIP), forming a pin-hole free perovskite nanocrystals in a thin-film matrix of PIP [41]. In the same year, 6.5% EQE LEDs were fabricated using uniform and compact OPA-CsPbBr$_3$ films [42]. EQEs up to 10.4% were also achieved with ultra-small grains (10 nm) and highly-uniform films with a surface roughness under 1 nm using a large-group ammonium halide to contain the growth of 3D perovskite grains during the film formation [37].

Meanwhile, a single-, double- or triple cation doping was shown to potentially improve both the device performance and stability into high-quality perovskite films [21,43–46]. Nevertheless, the poor stability of the perovskite itself under ambient conditions because of the extrinsic and intrinsic instabilities remains a major impediment towards commercialization [7,47–49]. As a result, the ambient environment processing causes rapid decomposition of the organo-inorganic halide perovskite material into optically-inert constituents, such as PbI$_2$ [50]. Tremendous efforts are underway in an attempt to address this problem and triple cation perovskite is widely recognized as a promising approach based on their lower sensitivity to processing conditions [51–53]. Most especially, the implementation of Cs+ as a third cation into the FA/MA perovskite is shown to improve both the stability and purity of the perovskite films [51,54,55]. FA/MA/Cs perovskite mixture can either crystallize into photoactive perovskite α-phase ("black phase") or non-photoactive non-perovskite hexagonal δ-phase ("yellow phase") [56–58]. For example, in FAPbI3 perovskite, its black perovskite contains a three-dimensional of corner linked PbI6 octahedra and its yellow perovskite has a linear chains of face-sharing octahedra. These chain-like structures are likely to hinder the electron transport through the materials [59]. These yellow phase impurities need to be avoided because they would limit the charge collection by influencing the crystal growths and the morphology of the perovskite [54]. The success of the MA/FA mixtures illustrates that smaller cation MA can be thought as a stabilizer for the black phase of the FA perovskite [60]. Cs has the smallest ionic radius of 1.81Å comparing to that of MA (2.70Å) and FA (2.79Å) [61]. Previous research had shown that incorporating Cs would improve the perovskite structural stability which would also effectively assists black phase crystallization in FA perovskite because of entropic stabilization [62]. Already, mixed cation perovskite (FA$_{(1-X)}$Cs$_X$PbBr$_3$) for LEDs, led to the first improvement in EQE from 0.82% to 1.82% using Cs cations [63]. Meanwhile, mixed cation FA$_X$MA$_{(1-X)}$PbBr$_3$ with quantum dots were also used to reach 3.5% in EQE [64]. The synthesis of Cs-containing triple cation perovskite nanocrystals with nominal stoichiometry Cs$_x$(MA$_{0.17}$FA$_{0.83}$)$_{1-x}$PbBr$_3$ (x = 0-0.15) were shown to yield LED devices with EQEs reaching 7.4% under argon-filled glovebox-controlled fabrication environment [21].

In this work, we demonstrate triple cation perovskite-based LED devices with the perovskite synthesis, device fabrication and operation all entirely performed under ambient conditions. As we show, compact triple cation perovskite films with large crystal grains are obtained using solvent treatment methods to produce near-infrared LEDs operating at 750 nm, with a maximum EQE reaching 3.1% ± 0.3%. In turn, we optimize the perovskite crystallinity, grain size and film thickness for LED integration using DMF (N,N-Dimethylmethanamide) added to the perovskite precursor. In doing so, we can achieve another ∼90% improvement in EQE to reach 5.9% ± 0.59% without altering the peak emission wavelength. We believe our triple cation perovskite synthesis and perovskite film optimization technique could significantly impact towards low-cost, stable and efficient solution-based LEDs.

2. Results and discussions

We first produce the perovskite films under ambient conditions by incorporating $Pb(SCN)_2$ (lead thiocyanate), and using solvent-antisolvent engineering technique to obtain the triple-cation perovskite $(Cs_x(MA_{0.17}FA_{0.83})Pb_{(100-x)}(I_{0.83}Br_{0.17})_3)$ precursor solution [65]. Solvent treatment using ethanol and chlorobenzene is known to promote the crystallization of the perovskite film [65,66]. The addition of thiocyanate (SCN-) does not alter the crystallographic structure since the ionic radius of SCN- (~0.217 nm) is akin to iodine ions (0.220 nm) [67]. The SCN− addition also results in more stable pseudo-halide perovskite formation due to the enhanced chemical bonding in the lattice [68]. The perovskite film synthesis is entirely described in the experimental section. Compared to photovoltaic devices, LED performances are greatly dependent on the characterizations of the active layer film including film thickness, film homogeneity and surface roughness. For thin perovskite layer, surface morphology is especially critical to avoid the current leakage. In addition, if the perovskite layer is too thin, the lack of active material would also limit the LED's emission. For thick films, none-radiative carrier recombination would be the major factor limiting the LED's emission. [69]. To reach optimal LED performances, we used DMF solvent into the perovskite precursor in order to achieve smaller grain sizes and thinner densely-packed perovskite films. The films morphology and crystalline structure are investigated using scanning electron microscope (SEM) and X-ray diffraction (XRD). SEM micrographs shown in Fig. 1(a-d) reveal the morphology of the perovskite films with different DMF volumes, namely: pristine (100% perovskite concentration), perovskite:DMF at 7:1 (87.5% perovskite concentration), 4:1 (80% perovskite concentration) and 2:1 (66.6% perovskite concentration) volume ratio respectively. All these precursor solutions are deposited atop a PEDOT: PSS (poly(3,4-ethylenedioxythiophene)-poly(styrenesulfonate) coated fluorine-doped tin oxide (FTO) substrate to mimic the final LED device architecture. Overall, the SEM micrographs in Fig. 1(a-d) reveal a complete and homogeneous coverage. The grain size ranging from ~90 nm to ~1.23 µm is measured by using ImageJ from the SEM images (detailed measurements and methods are provided in the Supplement 1). The average grain size and film thickness achieved for each precursor concentration are shown in Fig. 2, where 100%, 87.5%, 80% and 66.6% -rich precursors yield average crystallite grain diameters (and corresponding film thicknesses) of 674 ± 67.4 nm (290 ± 29 nm), 616 ± 61.6 nm (190 ± 19 nm), 537 ± 53.7 nm (160 ± 16 nm) and 402 ± 40.2 nm (100 ± 10 nm) respectively. These average grain size values are measured and calculated based on 50 randomly selected grain sizes for each sample. Because all the spin-coating and annealing parameters are the same for all the sample, the grain size variation could be caused by the difference in the solution concentration. The crystallite size estimated from XRD (Table 1) revealed that the 66.6% film has the largest crystallite size of 41.49 nm compared to that of 33.65 nm, 28.14 nm and 33.04 nm for the 100%, 87.5% and 80% samples respectively. Grain is either a single crystalline or polycrystalline material, and is presented either in bulk or thin film form. During the processing, smaller crystallites come closer and grow to become larger due to kinetics. Therefore, 66.6% sample has the smallest average gain size.

The XRD patterns in Fig. 3(a) indicate highly crystallized films. The perovskite materials crystallized in the tetragonal phase with space group I4cm(108) and lattice parameters a = b = 8.86 Å and c = 12.65 Å respectively [70,71]. The specific peaks at 14.15° (110) plane and 28.55° (220) plane are consistent for all the samples. Therefore, we can conclude that DMF additive shows no clear consequences on the XRD peaks shifting. **Table.1** summarizes the FWHM (full width at half maximum) values and the crystallite size in nm for all the samples at both 110 and 220. The full width at half-maximum (FWHM) of the (110) peak is estimated using Scherrer's equation. The FWHM of the (110) plane varied between 0.19° to 0.24°. Hence, the crystallinity of the perovskite films was evident even upon dilution and all the samples maintained the perovskite crystalline structure. The peak at 26.5° (marked as # in Fig. 3(a))corresponds to FTO substrate which is more pronounced in the 66.6% films due to the low thickness of the film. As the
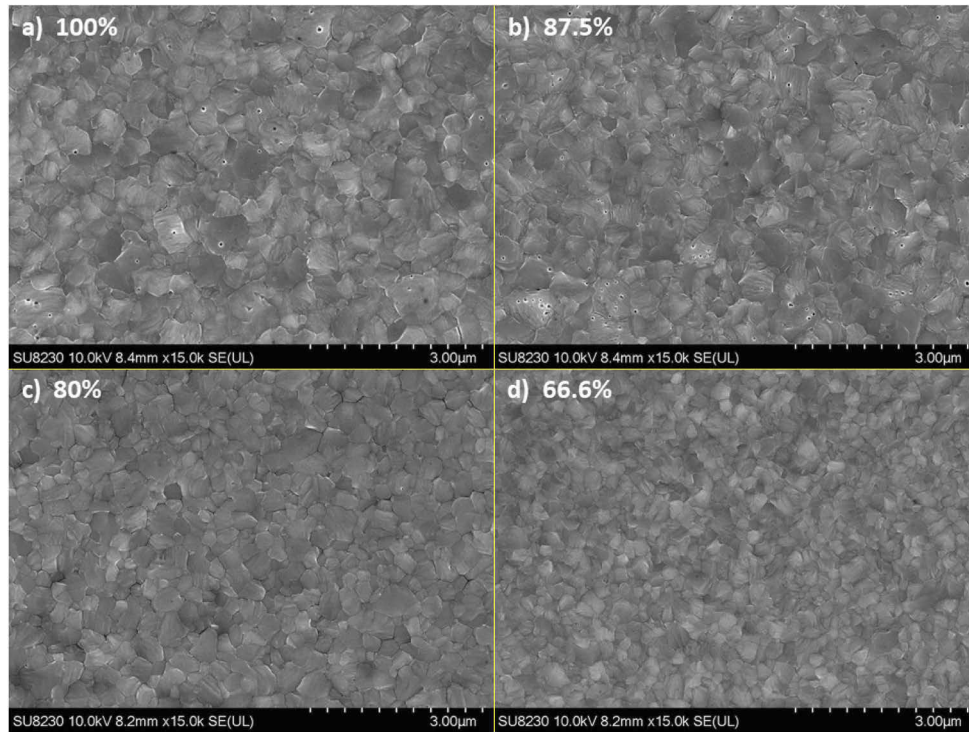
Fig. 1. SEM images of the perovskite surface with the scale bar at 3μm for films produced using a) 100%, b) 87.5%, c) 80%, and d) 66.6% precursor concentration, in volume percentage.
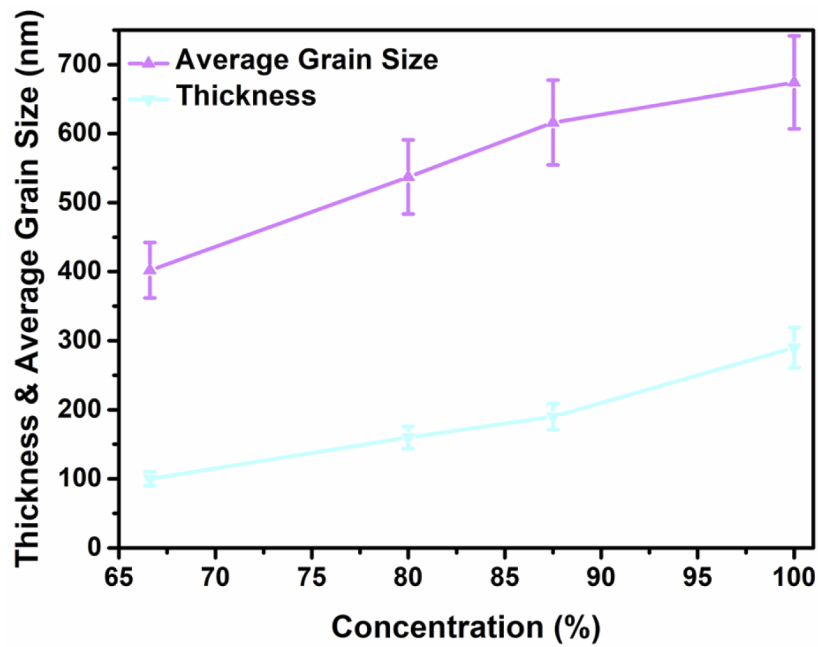

Fig. 2. Film thickness and average plots for each sample batch. The error bars for average grain size and thickness are 10% of their original values.

Table 1. The details about the FWHM and their calculated crystallite size are summarized in the table below:

Angle		FWHM	Crystallite size (nm)
100%			
14.11	**(110)**	0.23515	33.65007
28.52	**(220)**	0.33579	24.13005
87.5%		--	--
14.14	**(110)**	0.28118	28.1426
28.56	**(220)**	0.41317	19.61255
80%		--	--
14.13	**(110)**	0.23947	33.04377
28.54	**(220)**	0.31926	25.38002
66.6%		--	--
14.14	**(110)**	0.19069	41.4983
28.59	**(220)**	0.191	42.42834

thickness increases the intensity of this peak decreases. Tauc plots obtained by UV-visible optical absorption spectroscopy in Fig. 3(b) show that pristine perovskite has a bandgap at 1.68 ± 0.01 eV, while the DMF addition always yields the same bandgap within the margin of error.
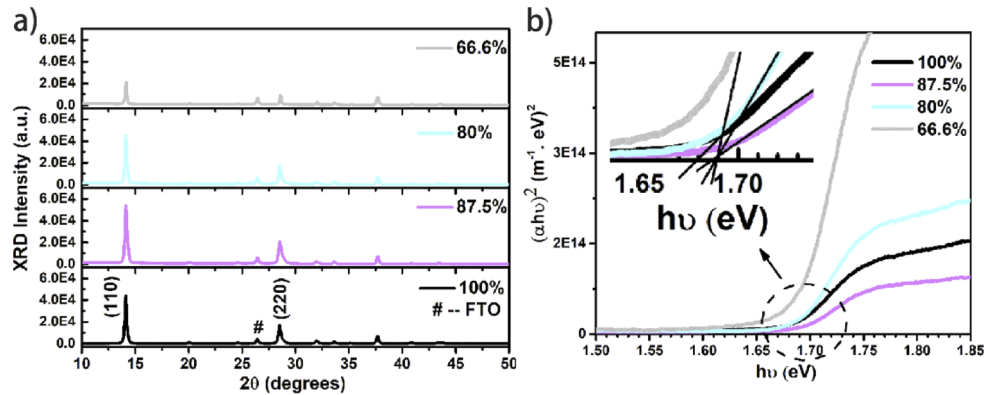

Fig. 3. a) X-ray diffraction patterns b) Tauc plot of the perovskite thin films with the different precursor concentrations. The inset highlights the band-gap assessments from the linear extrapolation.

In order to produce near-infrared perovskite-based LED devices, we use a simple three-layer architecture shown in Fig. 4(a) with the PEDOT:PSS/Perovskite/Poly(9,9-di-n-octylfluorenyl-2,7-diyl) (F8) conjugated polymer sandwiched between the FTO cathode and the MoO_3/Ag anode respectively. MoO_3/Ag has a high-workfunction and is used to provide ohmic hole injection into the device [72]. F8 is a polyfluorene conjugated polymer chosen to form a type-I heterojunction with the perovskite. This type-I heterojunction is able to be used as carrier-blocking material in order to prevent electrical shorts through the perovskite layer and emission-quenching at the contact interfaces [43,73]. Figure 4(b) shows the band diagram of the designed perovskite LED architecture.

Figure 5 presents a comparative statistical analysis of the electroluminescence intensity for multiple (over 50) LED devices produced using the different precursor concentrations (100%, 87.5%, 80% and 66.6%) in order to show the improvements of the fabricated devices are not the
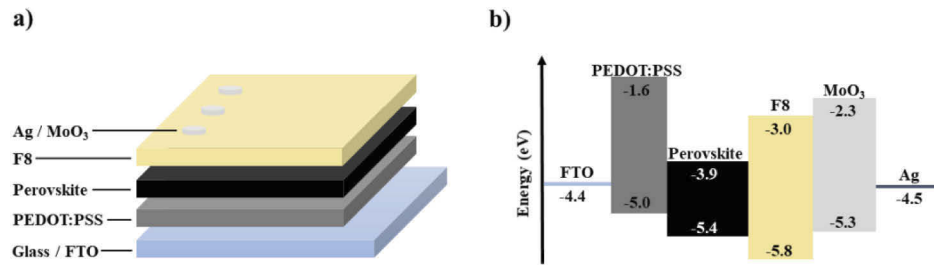
Fig. 4. (a) Schematic of the LED device structure. (b) Band-diagram of this LED architecture.

particular cases. At least 10 samples are analyzed for each precursor concentration, while all other operation parameters remain the same (active surface area, applied voltage applied, spectrometer slit and integration time). The grey boxes indicate the emission intensity range covering the 2nd and 3rd quartile (25%~75%), while the top and bottom bars present the extremums. This statistical analysis together combined with the thickness and grain distribution measurements from Fig. 2 suggest that 80% precursor concentration in DMF yields the best trade-off between the quality and thickness of the perovskite emitting layer. As the perovskite concentration is being further reduced by addition of DMF, their performance decreases significantly because of the decreased perovskite film crystallinity coupled with insufficient perovskite materials for light emission. However, the lower film thickness compared to the undiluted (100%) precursor concentration helps reduce carrier losses and provide a better carrier balance to favor the exciton formation and radiative emission.
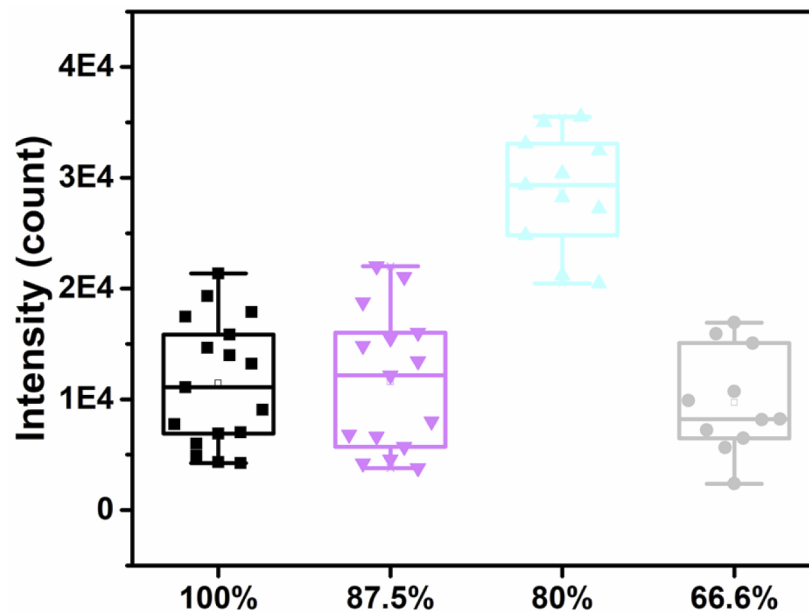

Fig. 5. Statistical analysis of the electroluminescence intensity for more than 50 devices in total. At least 10 devices are included for each perovskite precursor concentration. The grey box indicates the devices emitting within the 2nd and 3rd quartile (25%~75%) range. The solid line within the box represents the median for each device group.

The electroluminescence spectra under applied voltage of 4V in Fig. 6(a) are obtained for LEDs produced with perovskite films using the 100%, 87.5%, 80% and 66.6% precursor concentrations. Their emission peaks are respectively at 750, 751, 753 and 751+/- 2 nm, which is consistent with the bandgap values within the margins of error. Among these four different LEDs, the devices with the 80% precursor concentration yield a very significantly (3X) stronger emission compared with all others. This can be explained by the optimal trade-off between a better carrier delivery (a thinner film) compared with the 100% and 87.5% precursor concentrations, and a significantly better perovskite crystallinity than the 66.6% films. In addition, lower leakage current of the 80% device comparing to the rest as shown in Fig. 6(b) could also be another reason. The emission's FWHM for LEDs using the 80% precursor concentration is 40 nm.
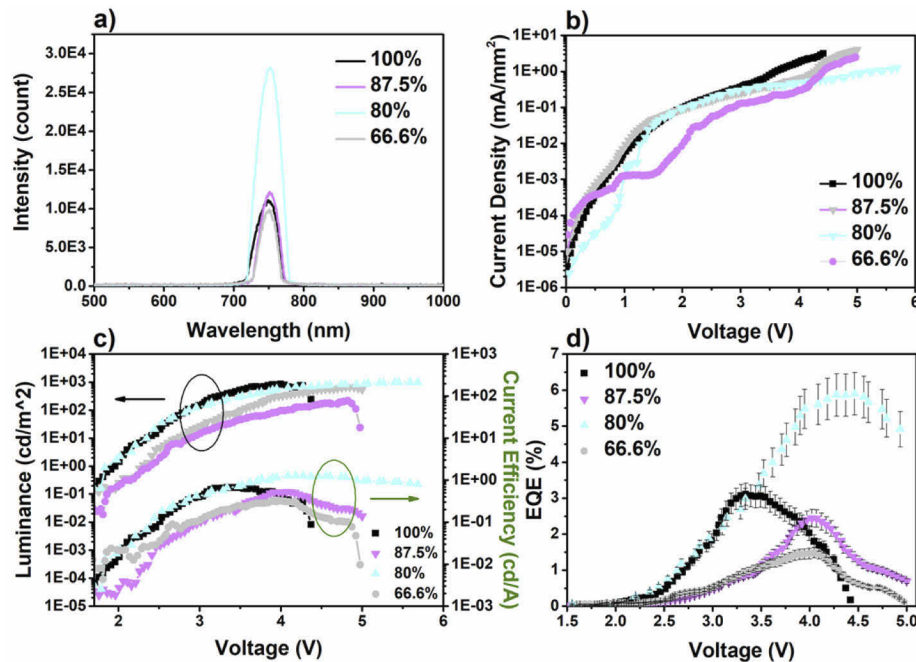

Fig. 6. Device characterizations for perovskite LEDs with different precursor concentrations 100%, 87.5%, 80% and 66.6%. a) Electroluminescence spectrum under a 4.5 V bias. b) Current density-voltage (J-V) device characteristics. c) External quantum efficiency (EQE)-voltage characteristics. d) Luminance-voltage characteristics.

The current density–voltage (J-V) characteristics in log scale of the best devices from each batch are shown in Fig. 6(b). Under applied voltage less than 1V, the 80% device exhibits the lowest current density comparing to the rest three devices suggesting 80% device has the lowest leakage current. The 100% device stops working at 4.2V and the 80% device has the highest working voltage of 5.7V. It may because 100% device has the highest perovskite layer thickness preventing carriers from drifting resulting reduced radiative recombination of the carriers. As it is for 66.6% device, number of carriers are greatly reduced because the dilution rate is too high. Figure 6(c) represents the device luminance and current efficiency as a function of applied voltage. The luminance of the 100% device drops dramatically after voltage exceeding 4V comparing to those of 87.5% and 66.6% at 4.8V. Perovskite LED with 80% precursor concentration exhibits the highest performance of 986 cd/m^2 in luminance and 1.26 cd/A in current efficiency, and continuing emitting until 5.7V. Figure 6(d) shows the EQE-voltage characteristics for all devices. The maximum EQE of these devices are 3.1% (100%), 2.4% (87.5%), 5.9% (80%) and 1.5%

(66.6%) with 10% data error values. The peak EQE of $5.9\% \pm 0.59\%$ achieved with the 80% precursor concentration represents a 90% increase in EQE comparing to that of the pristine 100% precursor concentration. It should be noticed that the device efficiency drops significantly at a higher perovskite volume ratio.

We have also use Table 2 to compare our results with the state-of-the-art literature using other mixed cation or triple cation perovskite-based LEDs.

Table 2. Comaparision of the present work with the recent mixed cation or triple cation perovskite-based LEDs.

Device Structure	Perovskite Emitter	V_{on} (V)	(nm)	Max EQE (%)	Ref.
FTO/PEDOT:PSS/Perovskite/ F8/MoO$_3$/Ag	$(Cs_x(MA_{0.17}FA_{0.83}) Pb_{(100-x)}(I_{0.83}Br_{0.17})_3)$	3	750	5.4 ~6.5	This work
ITO/PEDOT:PSS/ Poly-TPD/Perovskite/ POT-2 T/LiF/Al	$Cs_x(MA_{0.17}FA_{0.83})_{1-x}PbBr_3$ $(x = 0–0.05)$.	1.98	523	7.36	[21]
ITO/PEDOT:PSS/TFB/ Perovskite/TPBi/LiF/Al	$FA_{0.8}Cs_{0.2}PbBr_3$	3.5	520 ~ 535	~2.8	[63]
ITO/PEODOT:PSS/TFB/ Perovskite/TPBi/LiF/Al	$MA_{0.8}Cs_{0.2}PbBr_3$	3.0	523	1.3	[74]
ITO/PEDOT:PSS/poly- TPD/Perovskite /TPBi/LiF/Al	$CsPb_{1-x}Sn_xBr_3$	5.0	508	N/A	[75]
ITO/AZO/AZO:Cs/Perovskite/ CuS-GaSnO/WO$_3$/Au	$Cs_{10}(MA_{0.1}7FA_{0.83})_{(100-x)} Pb(Br_xI_{1-x})_3$	2.5 2.7 3.1	569 650 475	12.98 8.21 2.58	[76]
ITO/ZnO/PVA/Perovskite/ PVK/MoO$_3$/Al	$Cs_{0.76}FA_{0.24}PbBr_3$.	2.6	~535	3.8	[77]

3.　Experimental methods

The precursor solutions were prepared from chemicals purchased from Sigma Aldrich and Ossila unless stated otherwise. The complete perovskite synthesis and device fabrication steps are performed in ambient conditions (in air) at 22°C and 50% relative humidity. The triple-cation perovskite is prepared by adding lead thiocyanate to make it more stable under ambient conditions [78]. 0.6M-MAI, 0.2M-MABr, 1M-FAI, 0.8 M-PbI$_2$ and 0.5M-PbBr$_2$ are all dissolved in 4:1 DMF:DMSO (volume ratio) [78]. This is followed by the addition of a 70 µl cesium iodide solution to the perovskite solution and stirring slowly for 60 minutes without heating. During the thin-film deposition, we optimize the morphology and grain size using solvent-anti-solvent (ethanol and chlorobenzene) treatment previously reported [65]. For the fabrication of the LEDs, the perovskite solution is further modified by adding different volume ratios of anhydrous DMF (N,N-Dimethylformamide) to obtain perovskite precursors : DMF at 7:1 (87.5%), 4:1 (80%) and 2:1 (66.6%) volume ratio (dilution). These solutions are used to fabricate all the devices presented in this work.

For deposition, the fluorine doped-tin oxide (FTO) substrates (Ossila S304, 12~14 Ω/sq) are ultrasonically cleaned in sequence using acetone and isopropanol for 10 minutes each. PEDOT: PSS (CleviosTM P VP AI 4083) diluted with isopropanol (1:3 volume ratio) is spin-coated directly atop of the FTO substrate at 3000 rpm for 40s and annealed at 200°C for 15 minutes in air. The thickness of the PEDOT:PSS layer is ~150nm. Before perovskite deposition, the FTO glasses coated with PEDOT: PSS are exposed under a UV-lamp (405nm, 6W) for 15 minutes to improve the wettability for perovskite deposition. After the UV treatment, the perovskite

precursor solution is spin-coated atop the PEDOT: PSS in dynamic mode at 2000 rpm for 20s, followed by the solvent-anti-solvent (ethanol and chlorobenzene) treatment at 5000 rpm for 20s to achieve a compact and well crystallized thin film [65]. The samples are subsequently annealed at 125°C for 15 minutes on a hotplate in air for the perovskite conversion. After cooling-down, poly(9,9-di-n-octylfluorenyl-2,7-diyl) (F8) (Sigma-Aldrich) is diluted at a concentration of 10mg/ml in chlorobenzene before spin-coating atop the perovskite layer at 4000 rpm for 30s. The samples are subsequently annealed at 80°C for 15 minutes and cooled-down to room temperature. Finally, a 5-nm MoO_3 layer is thermally evaporated atop the F8 conjugated polymer layer at 0.2Å/s, followed by a 150-nm thick thermally evaporated silver electrode deposition through a 0.025 cm^2 round-shaped shadow mask at 0.2 Å/s.

The SEM images are acquired using a Hitachi SU 8230 ultra-high-resolution field emission scanning electron microscope. XRD patterns were obtained using a Bruker-AXS D8 Advance X-ray diffractometer with CuKα1 source (λ = 1.5406 Å). UV–vis optical absorption spectrum is measured using a UV–vis–NIR, PerkinElmer Lamba 750 spectrophotometer. An Ambios XP200 profilometer is used to measure the thickness of the perovskite films, using a scanning speed of 0.03mm/s and a 0.03mg stylus force.

Steady-state electroluminescence (EL) spectra are recorded using a Jobin-Yvon iHR320 triple-grating spectrometer equipped with a Synapse silicon CCD array. The perovskite LED emitting power is measured using a photodetector (Thorlabs, S120VC, 200-1100nm, 50mW) connected through a power and energy meter module (Thorlabs, model PM100USB), and the current-voltage (IV) characteristics are measured using a Keithley 2400 source-measure unit (SMU) controlled with LabVIEW. The power and IV measurements are performed at the same time, so that the external quantum efficiency (EQE) could be directly calculated from the equation below:

$$EQE = \frac{n(photon)}{n(electron)} = \frac{P/E(photon)}{I/q}$$

where P is measured power, I is measured corresponding current, q is electron charge and E(photon) is calculated by 1.2398/λ(um) which λ is the peak wavelength.

4.   Conclusions

In summary, we describe a triple cation perovskite synthesis method customized for the fabrication of efficient near-infrared LEDs. All the devices are produced in air at room-temperature by incorporating thiocyanate ions and using a solvent-antisolvent treatment method. Because this precursor chemistry is much more commonly used for photovoltaic devices, we demonstrate that we can significantly improve the EQE of our LED devices from 3.1% to 5.9% by diluting this precursor with DMF. This can allow us to optimize the key characteristics of the perovskite films for LED applications, by reducing both the grain size and the film thickness, while preserving a sound crystalline structure consistent with the tetragonal halide perovskite polymorph. By far, the best LED devices are fabricated with using a 80% perovskite precursor concentration in DMF to achieve a maximum EQE of 5.9%. As such, we believe that this paper represents an important step towards new low-cost perovskite-based LED devices and technologies for a wide range of applications including energy-efficient lighting, biosensing and displays

Data availability. Data underlying the results presented in this paper are not publicly available at this time but may be obtained from the authors upon reasonable request.

Supplemental document. See Supplement 1 for supporting content.

References

1. J. Chen, S. Zhou, S. Jin, H. Li, and T. Zhai, "Crystal organometal halide perovskites with promising optoelectronic applications," J. Mater. Chem. C **4**(1), 11–27 (2016).
2. W. Zhang, G. E. Eperon, and H. J. Snaith, "Metal halide perovskites for energy applications," Nat. Energy **1**(6), 1–8 (2016).
3. M. Konstantakou and T. Stergiopoulos, "A critical review on tin halide perovskite solar cells," J. Mater. Chem. A **5**(23), 11518–11549 (2017).
4. W.-J. Yin, J.-H. Yang, J. Kang, Y. Yan, and S.-H. Wei, "Halide perovskite materials for solar cells: a theoretical review," J. Mater. Chem. A **3**(17), 8926–8942 (2015).
5. S. Zhou, R. Tang, and L. Yin, "Slow-photon-effect-induced photoelectrical-conversion efficiency enhancement for carbon-quantum-dot-sensitized inorganic $CsPbBr_3$ inverse opal perovskite solar cells," Adv. Mater. **29**(43), 1703682 (2017).
6. Q. V. Le, H. W. Jang, and S. Y. Kim, "Recent advances toward high-efficiency halide perovskite light-emitting diodes: review and perspective," Small Methods **2**(10), 1700419 (2018).
7. Z. Yang, B. H. Babu, S. Wu, T. Liu, S. Fang, Z. Xiong, L. Han, and W. Chen, "Review on practical interface engineering of perovskite solar cells: from efficiency to stability," Sol. RRL **4**(2), 1900257 (2020).
8. S. Liu, Y. Guan, Y. Sheng, Y. Hu, Y. Rong, A. Mei, and H. Han, "A review on additives for halide perovskite solar cells," Adv. Energy Mater. **10**(13), 1902492 (2020).
9. C. Zhang, D.-B. Kuang, and W.-Q. Wu, "A review of diverse halide perovskite morphologies for efficient optoelectronic applications," Small Methods **4**(2), 1900662 (2020).
10. A. Kojima, K. Teshima, Y. Shirai, and T. Miyasaka, "Organometal halide perovskites as visible-light sensitizers for photovoltaic cells," J. Am. Chem. Soc. **131**(17), 6050–6051 (2009).
11. M. A. Green, E. D. Dunlop, J. Hohl-Ebinger, M. Yoshita, N. Kopidakis, and A. W. Y. Ho-Baillie, "Solar cell efficiency tables (Version 55)," Prog Photovolt Res Appl **28**(1), 3–15 (2020).
12. H. Dong, C. Zhang, X. Liu, J. Yao, and Y. S. Zhao, "Materials chemistry and engineering in metal halide perovskite lasers," Chem. Soc. Rev. **49**(3), 951–982 (2020).
13. Q. Shang, M. Li, L. Zhao, D. Chen, S. Zhang, S. Chen, P. Gao, C. Shen, J. Xing, G. Xing, B. Shen, X. Liu, and Q. Zhang, "Role of the exciton–polariton in a continuous-wave optically pumped $CsPbBr_3$ perovskite laser," Nano Lett. **20**(9), 6636–6643 (2020).
14. S. Tong, C. Gong, C. Zhang, G. Liu, D. Zhang, C. Zhou, J. Sun, S. Xiao, J. He, Y. Gao, and J. Yang, "Fully-printed, flexible cesium-doped triple cation perovskite photodetector," Applied Materials Today **15**, 389–397 (2019).
15. D. Liu, B.-B. Yu, M. Liao, Z. Jin, L. Zhou, X. Zhang, F. Wang, H. He, T. Gatti, and Z. He, "Self-powered and broadband lead-free inorganic perovskite photodetector with high stability," ACS Appl. Mater. Interfaces **12**(27), 30530–30537 (2020).
16. H. Jing, R. Peng, R.-M. Ma, J. He, Y. Zhou, Z. Yang, C.-Y. Li, Y. Liu, X. Guo, Y. Zhu, D. Wang, J. Su, C. Sun, W. Bao, and M. Wang, "Flexible ultrathin single-crystalline perovskite photodetector," Nano Lett. **20**(10), 7144–7151 (2020).
17. X.-K. Liu, W. Xu, S. Bai, Y. Jin, J. Wang, R. H. Friend, and F. Gao, "Metal halide perovskites for light-emitting diodes," Nat. Mater. **20**(1), 1–12 (2020).
18. Q. Shan, J. Song, Y. Zou, J. Li, L. Xu, J. Xue, Y. Dong, B. Han, J. Chen, and H. Zeng, "High performance metal halide perovskite light-emitting diode: from material design to device optimization," Small **13**(45), 1701770 (2017).
19. H. Cho, Y.-H. Kim, C. Wolf, H.-D. Lee, and T.-W. Lee, "Improving the stability of metal halide perovskite materials and light-emitting diodes," Adv. Mater. **30**(42), 1704587 (2018).
20. E. Ercan, P.-C. Tsai, J.-Y. Chen, J.-Y. Lam, L.-C. Hsu, C.-C. Chueh, and W.-C. Chen, "Stretchable and ambient stable perovskite/polymer luminous hybrid nanofibers of multicolor fiber mats and their white LED applications," ACS Appl. Mater. Interfaces **11**(26), 23605–23615 (2019).
21. P. Vashishtha, S. A. Veldhuis, S. S. H. Dintakurti, N. L. Kelly, B. E. Griffith, A. A. M. Brown, M. S. Ansari, A. Bruno, N. Mathews, Y. Fang, T. White, S. G. Mhaisalkar, and J. V. Hanna, "Investigating the structure–function relationship in triple cation perovskite nanocrystals for light-emitting diode applications," J. Mater. Chem. C **8**(34), 11805–11821 (2020).
22. P. Vashishtha, A. A. M. Brown, S. H. Pu, S. Mhaisalkar, and N. Mathews, "Tunable electroluminescence for pure white emission from a perovskite-based LED," Adv. Electron. Mater. **7**(4), 2001227 (2021).
23. N. Wang, L. Cheng, R. Ge, S. Zhang, Y. Miao, W. Zou, C. Yi, Y. Sun, Y. Cao, R. Yang, Y. Wei, Q. Guo, Y. Ke, M. Yu, Y. Jin, Y. Liu, Q. Ding, D. Di, L. Yang, G. Xing, H. Tian, C. Jin, F. Gao, R. H. Friend, J. Wang, and W. Huang, "Perovskite light-emitting diodes based on solution-processed self-organized multiple quantum wells," Nat. Photonics **10**(11), 699–704 (2016).
24. L. Zhao, K. M. Lee, K. Roh, S. U. Z. Khan, and B. P. Rand, "Improved outcoupling efficiency and stability of perovskite light-emitting diodes using thin emitting layers," Adv. Mater. **31**(2), 1805836 (2019).
25. B. R. Sutherland and E. H. Sargent, "Perovskite photonic sources," Nat. Photonics **10**(5), 295–302 (2016).

26. L. Zhang, X. Yang, Q. Jiang, P. Wang, Z. Yin, X. Zhang, H. Tan, Y. (Michael) Yang, M. Wei, B. R. Sutherland, E. H. Sargent, and J. You, "Ultra-bright and highly efficient inorganic based perovskite light-emitting diodes," Nat. Commun. **8**(1), 15640 (2017).

27. X. Zhao, J. D. A. Ng, R. H. Friend, and Z.-K. Tan, "Opportunities and challenges in perovskite light-emitting devices," ACS Photonics **5**(10), 3866–3875 (2018).

28. P. Vashishtha, S. Bishnoi, C.-H. A. Li, M. Jagadeeswararao, T. J. N. Hooper, N. Lohia, S. B. Shivarudraiah, M. S. Ansari, S. N. Sharma, and J. E. Halpert, "Recent advancements in near-infrared perovskite light-emitting diodes," ACS Appl. Electron. Mater. **2**(11), 3470–3490 (2020).

29. X. Zhao and Z.-K. Tan, "Large-area near-infrared perovskite light-emitting diodes," Nat. Photonics **14**(4), 215–218 (2020).

30. W. Xu, Q. Hu, S. Bai, C. Bao, Y. Miao, Z. Yuan, T. Borzda, A. J. Barker, E. Tyukalova, Z. Hu, M. Kawecki, H. Wang, Z. Yan, X. Liu, X. Shi, K. Uvdal, M. Fahlman, W. Zhang, M. Duchamp, J.-M. Liu, A. Petrozza, J. Wang, L.-M. Liu, W. Huang, and F. Gao, "Rational molecular passivation for high-performance perovskite light-emitting diodes," Nat. Photonics **13**(6), 418–424 (2019).

31. H. Wang, X. Zhang, Q. Wu, F. Cao, D. Yang, Y. Shang, Z. Ning, W. Zhang, W. Zheng, Y. Yan, S. V. Kershaw, L. Zhang, A. L. Rogach, and X. Yang, "Trifluoroacetate induced small-grained CsPbBr$_3$ perovskite films result in efficient and stable light-emitting devices," Nat. Commun. **10**(1), 665 (2019).

32. T. C. Sum and N. Mathews, *Halide Perovskites: Photovoltaics, Light Emitting Devices, and Beyond* (WILEY-VCH, n.d.).

33. L. N. Quan, F. P. G. de Arquer, R. P. Sabatini, and E. H. Sargent, "Perovskites for light emission," Adv. Mater. **30**(45), 1801996 (2018).

34. H. Cho, S.-H. Jeong, M.-H. Park, Y.-H. Kim, C. Wolf, C.-L. Lee, J. H. Heo, A. Sadhanala, N. Myoung, S. Yoo, S. H. Im, R. H. Friend, and T.-W. Lee, "Overcoming the electroluminescence efficiency limitations of perovskite light-emitting diodes," Science **350**(6265), 1222–1225 (2015).

35. L. Zhao, N. Rolston, K. M. Lee, X. Zhao, M. A. Reyes-Martinez, N. L. Tran, Y.-W. Yeh, N. Yao, G. D. Scholes, Y.-L. Loo, A. Selloni, R. H. Dauskardt, and B. P. Rand, "Influence of bulky organo-ammonium halide additive choice on the flexibility and efficiency of perovskite light-emitting devices," Adv. Funct. Mater. **28**(31), 1802060 (2018).

36. H. Tsai, W. Nie, P. Cheruku, N. H. Mack, P. Xu, G. Gupta, A. D. Mohite, and H.-L. Wang, "Optimizing composition and morphology for large-grain perovskite solar cells via chemical control," Chem. Mater. **27**(16), 5570–5576 (2015).

37. Z. Xiao, R. A. Kerner, L. Zhao, N. L. Tran, K. M. Lee, T.-W. Koh, G. D. Scholes, and B. P. Rand, "Efficient perovskite light-emitting diodes featuring nanometre-sized crystallites," Nat. Photonics **11**(2), 108–115 (2017).

38. H. Lin, L. Zhu, H. Huang, C. J. Reckmeier, C. Liang, A. L. Rogach, and W. C. H. Choy, "Efficient near-infrared light-emitting diodes based on organometallic halide perovskite–poly(2-ethyl-2-oxazoline) nanocomposite thin films," Nanoscale **8**(47), 19846–19852 (2016).

39. S.-H. Chin, J. W. Choi, H. C. Woo, J. H. Kim, H. S. Lee, and C.-L. Lee, "Realizing a highly luminescent perovskite thin film by controlling the grain size and crystallinity through solvent vapour annealing," Nanoscale **11**(13), 5861–5867 (2019).

40. K. Z. Swe, A. Naikaew, P. Kaewurai, P. Pansa-Ngat, S. Sahasithiwat, L. Kangkaew, S. Rugmai, S. Soontaranon, P. Kanjanaboos, and P. Kanjanaboos, "Layered perovskite with compact morphology and reduced grain size via vacuum assisted crystallization for luminescence applications," Opt. Mater. Express **10**(5), 1182–1192 (2020).

41. G. Li, Z.-K. Tan, D. Di, M. L. Lai, L. Jiang, J. H.-W. Lim, R. H. Friend, and N. C. Greenham, "Efficient light-emitting diodes based on nanocrystalline perovskite in a dielectric polymer matrix," Nano Lett. **15**(4), 2640–2644 (2015).

42. Y. Tan, Y. Zou, L. Wu, Q. Huang, D. Yang, M. Chen, M. Ban, C. Wu, T. Wu, S. Bai, T. Song, Q. Zhang, and B. Sun, "Highly luminescent and stable perovskite nanocrystals with octylphosphonic acid as a ligand for efficient light-emitting diodes," ACS Appl. Mater. Interfaces **10**(4), 3784–3792 (2018).

43. Z.-K. Tan, R. S. Moghaddam, M. L. Lai, P. Docampo, R. Higler, F. Deschler, M. Price, A. Sadhanala, L. M. Pazos, D. Credgington, F. Hanusch, T. Bein, H. J. Snaith, and R. H. Friend, "Bright light-emitting diodes based on organometal halide perovskite," Nature Nanotech **9**(9), 687–692 (2014).

44. H. Cho, J. S. Kim, C. Wolf, Y.-H. Kim, H. J. Yun, S.-H. Jeong, A. Sadhanala, V. Venugopalan, J. W. Choi, C.-L. Lee, R. H. Friend, and T.-W. Lee, "High-efficiency polycrystalline perovskite light-emitting diodes based on mixed cations," ACS Nano **12**(3), 2883–2892 (2018).

45. H. P. Kim, J. Kim, B. S. Kim, H.-M. Kim, J. Kim, A. R. bin, M. Yusoff, J. Jang, and M. K. Nazeeruddin, "High-efficiency, blue, green, and near-infrared light-emitting diodes based on triple cation perovskite," Adv. Opt. Mater. **5**(7), 1600920 (2017).

46. Z. Yi, "Stability study in lead-halide perovskite light-emitting diodes," Thesis, University of Cambridge (2021).

47. Y.-Y. Zhang, S. Chen, P. Xu, H. Xiang, X.-G. Gong, A. Walsh, and S.-H. Wei, "Intrinsic instability of the hybrid halide perovskite semiconductor CH$_3$NH$_3$PbI$_3$," Chinese Phys. Lett. **35**(3), 036104 (2018).

48. N. Arora, M. I. Dar, M. Abdi-Jalebi, F. Giordano, N. Pellet, G. Jacopin, R. H. Friend, S. M. Zakeeruddin, and M. Grätzel, "Intrinsic and extrinsic stability of formamidinium lead bromide perovskite solar cells yielding high photovoltage," Nano Lett. **16**(11), 7155–7162 (2016).

49. F. El-Mellouhi, E. T. Bentria, S. N. Rashkeev, S. Kais, and F. H. Alharbi, "Enhancing intrinsic stability of hybrid perovskite solar cell by strong, yet balanced, electronic coupling," Sci. Rep. **6**(1), 30305 (2016).

50. T. A. Berhe, W.-N. Su, C.-H. Chen, C.-J. Pan, J.-H. Cheng, H.-M. Chen, M.-C. Tsai, L.-Y. Chen, A. A. Dubale, and B.-J. Hwang, "Organometal halide perovskite solar cells: degradation and stability," Energy Environ. Sci. **9**(2), 323–356 (2016).

51. M. Stolterfoht, C. M. Wolff, Y. Amir, A. Paulke, L. Perdigón-Toro, P. Caprioglio, and D. Neher, "Approaching the fill factor Shockley–Queisser limit in stable, dopant-free triple cation perovskite solar cells," Energy Environ. Sci. **10**(6), 1530–1539 (2017).

52. C. Wang, C. Zhang, S. Wang, G. Liu, H. Xia, S. Tong, J. He, D. Niu, C. Zhou, K. Ding, Y. Gao, and J. Yang, "Low-temperature processed, efficient, and highly reproducible cesium-doped triple cation perovskite planar heterojunction solar cells," Sol. RRL **2**(2), 1700209 (2018).

53. Y. Wang, J. Wu, P. Zhang, D. Liu, T. Zhang, L. Ji, X. Gu, Z. David Chen, and S. Li, "Stitching triple cation perovskite by a mixed anti-solvent process for high performance perovskite solar cells," Nano Energy **39**, 616–625 (2017).

54. M. Saliba, T. Matsui, J.-Y. Seo, K. Domanski, J.-P. Correa-Baena, M. K. Nazeeruddin, S. M. Zakeeruddin, W. Tress, A. Abate, A. Hagfeldt, and M. Grätzel, "Cesium-containing triple cation perovskite solar cells: improved stability, reproducibility and high efficiency," Energy Environ. Sci. **9**(6), 1989–1997 (2016).

55. M. Azam, S. Yue, R. Xu, K. Liu, K. Ren, Y. Sun, J. Liu, Z. Wang, S. Qu, Y. Lei, and Z. Wang, "Highly efficient solar cells based on Cl incorporated tri-cation perovskite materials," J. Mater. Chem. A **6**(28), 13725–13734 (2018).

56. C. C. Stoumpos, C. D. Malliakas, and M. G. Kanatzidis, "Semiconducting tin and lead iodide perovskites with organic cations: phase transitions, high mobilities, and near-infrared photoluminescent properties," Inorg. Chem. **52**(15), 9019–9038 (2013).

57. G. E. Eperon, S. D. Stranks, C. Menelaou, M. B. Johnston, L. M. Herz, and H. J. Snaith, "Formamidinium lead trihalide: a broadly tunable perovskite for efficient planar heterojunction solar cells," Energy Environ. Sci. **7**(3), 982–988 (2014).

58. J.-W. Lee, D.-J. Seol, A.-N. Cho, and N.-G. Park, "High-efficiency perovskite solar cells based on the black polymorph of $HC(NH_2)_2 PbI_3$," Adv Mater **26**(29), 4991–4998 (2014).

59. T. M. Koh, K. Fu, Y. Fang, S. Chen, T. C. Sum, N. Mathews, S. G. Mhaisalkar, P. P. Boix, and T. Baikie, "Formamidinium-containing metal-halide: an alternative material for near-IR absorption perovskite solar cells," J. Phys. Chem. C **118**(30), 16458–16462 (2014).

60. N. Pellet, P. Gao, G. Gregori, T.-Y. Yang, M. K. Nazeeruddin, J. Maier, and M. Grätzel, "Mixed-organic-cation perovskite photovoltaics for enhanced solar-light harvesting," Angew. Chem. Int. Ed. **53**(12), 3151–3157 (2014).

61. A. Amat, E. Mosconi, E. Ronca, C. Quarti, P. Umari, Md. K. Nazeeruddin, M. Grätzel, and F. De Angelis, "Cation-induced band-gap tuning in organohalide perovskites: interplay of spin–orbit coupling and octahedra tilting," Nano Lett. **14**(6), 3608–3616 (2014).

62. C. Yi, J. Luo, S. Meloni, A. Boziki, N. Ashari-Astani, C. Grätzel, S. M. Zakeeruddin, U. Röthlisberger, and M. Grätzel, "Entropic stabilization of mixed A-cation ABX_3 metal halide perovskites for high performance perovskite solar cells," Energy Environ. Sci. **9**(2), 656–662 (2016).

63. X. Zhang, H. Liu, W. Wang, J. Zhang, B. Xu, K. L. Karen, Y. Zheng, S. Liu, S. Chen, K. Wang, and X. W. Sun, "Hybrid perovskite light-emitting diodes based on perovskite nanocrystals with organic–inorganic mixed cations," Adv. Mater. **29**(18), 1606405 (2017).

64. B. Xu, W. Cao, X. Zhang, W. Wang, J. Hao, S. Chen, K. Wang, and X. Sun, "Efficient perovskite light-emitting diodes based on double organic cations," in *2017 Conference on Lasers and Electro-Optics (CLEO)* (2017), pp. 1–2.

65. D. Gedamu, I. M. Asuo, D. Benetti, M. Basti, I. Ka, S. G. Cloutier, F. Rosei, and R. Nechache, "Solvent-antisolvent ambient processed large grain size perovskite thin films for high-performance solar cells," Sci. Rep. **8**(1), 12885 (2018).

66. J. M. Kadro, N. Pellet, F. Giordano, A. Ulianov, O. Müntener, J. Maier, M. Grätzel, and A. Hagfeldt, "Proof-of-concept for facile perovskite solar cell recycling," Energy Environ. Sci. **9**(10), 3172–3179 (2016).

67. A. Halder, R. Chulliyil, A. S. Subbiah, T. Khan, S. Chattoraj, A. Chowdhury, and S. K. Sarkar, "Pseudohalide (SCN–)-doped $MAPbI_3$ perovskites: a few surprises," J. Phys. Chem. Lett. **6**(17), 3483–3489 (2015).

68. Q. Jiang, D. Rebollar, J. Gong, E. L. Piacentino, C. Zheng, and T. Xu, "Pseudohalide-induced moisture tolerance in perovskite $CH_3NH_3Pb(SCN)2I$ Thin Films," Angew. Chem. **127**(26), 7727–7730 (2015).

69. D. Liu, M. K. Gangishetty, and T. L. Kelly, "Effect of $CH_3NH_3PbI_3$ thickness on device efficiency in planar heterojunction perovskite solar cells," J. Mater. Chem. A **2**(46), 19873–19881 (2014).

70. H.-S. Kim, S. H. Im, and N.-G. Park, "Organolead halide perovskite: new horizons in solar cell research," J. Phys. Chem. C **118**(11), 5615–5625 (2014).

71. I. M. Asuo, D. Gedamu, I. Ka, L. F. Gerlein, F.-X. Fortier, A. Pignolet, S. G. Cloutier, and R. Nechache, "High-performance pseudo-halide perovskite nanowire networks for stable and fast-response photodetector," Nano Energy **51**, 324–332 (2018).

72. L.-P. Lu, D. Kabra, K. Johnson, and R. H. Friend, "Charge-carrier balance and color purity in polyfluorene polymer blends for blue light-emitting diodes," Adv. Funct. Mater. **22**(1), 144–150 (2012).

73. R. L. Z. Hoye, M. R. Chua, K. P. Musselman, G. Li, M.-L. Lai, Z.-K. Tan, N. C. Greenham, J. L. MacManus-Driscoll, R. H. Friend, and D. Credgington, "Enhanced performance in fluorene-free organometal halide perovskite light-emitting diodes using tunable, low electron affinity oxide electron injectors," Adv. Mater. **27**(8), 1414–1419 (2015).

74. B. Xu, W. Wang, X. Zhang, W. Cao, D. Wu, S. Liu, H. Dai, S. Chen, K. Wang, and X. Sun, "Bright and efficient light-emitting diodes based on MA/Cs double cation perovskite nanocrystals," J. Mater. Chem. C **5**(25), 6123–6128 (2017).

75. A. Giuri, Z. Yuan, Y. Miao, J. Wang, F. Gao, N. Sestu, M. Saba, G. Bongiovanni, S. Colella, C. E. Corcione, G. Gigli, A. Listorti, and A. Rizzo, "Ultra-bright near-infrared perovskite light-emitting diodes with reduced efficiency roll-off," Sci. Rep. **8**(1), 15496 (2018).

76. A. R. B. M. Yusoff, A. E. X. Gavim, A. G. Macedo, W. J. da Silva, F. K. Schneider, and M. A. M. Teridi, "High-efficiency, solution-processable, multilayer triple cation perovskite light-emitting diodes with copper sulfide–gallium–tin oxide hole transport layer and aluminum-zinc oxide–doped cesium electron injection layer," Materials Today Chemistry **10**, 104–111 (2018).

77. G. Xie, C. Jiang, J. Wang, C. Mai, G. Huang, Y. Ma, J. Wang, J. Peng, and Y. Cao, "Stable mixed-cation perovskite light-emitting diodes," Org. Electron. **71**, 58–64 (2019).

78. I. M. Asuo, D. Gedamu, N. Y. Doumon, I. Ka, A. Pignolet, S. G. Cloutier, and R. Nechache, "Ambient condition-processing strategy for improved air-stability and efficiency in mixed-cation perovskite solar cells," Mater. Adv. **1**(6), 1866–1876 (2020).